Layered mantle heterogeneities associated with post-subducted slab segments

Youqiang Yu [a],*, Zhiguo Xu [b], Stephen S. Gao [c], Kelly H. Liu [c], Jia Gao [a]

[a] *State Key Laboratory of Marine Geology, Tongji University, Shanghai, 200092, China*
[b] *National Marine Environmental Forecasting Center, Beijing, 100081, China*
[c] *Geology and Geophysics Program, Missouri University of Science and Technology, Rolla, MO 65409, USA*

ARTICLE INFO

ABSTRACT

The South China Sea (SCS) is a hydrocarbon-rich major marginal sea in the western Pacific Ocean. One of the proposed driving mechanisms for its formation is the slab-pull of a Mesozoic ocean basin known as the Proto-South China Sea (PSCS), which subducted beneath northern Borneo between the Eocene and the early Miocene. However, the present-day depth extent of the slabs and even the existence of the PSCS remain highly debated. By stacking P-to-S conversions from the 410 km and 660 km discontinuities bordering the mantle transition zone (MTZ), we demonstrate significant MTZ thickening beneath the southern margin of the SCS, which, when combined with previously-revealed high-velocity anomalies in the MTZ, provides evidence for the existence of the PSCS. Chemically and rheologically heterogeneous materials segregated from the slab segments may have generated layered structures as evidenced by the discontinuities observed at the depths of ∼350 km and ∼730 km. Dehydration melting from the slab segments may be a viable mechanism for the extensive post-spreading magmatism in the southern SCS.

© 2021 Elsevier B.V. All rights reserved.

1. Introduction

Subduction is one of the first-order tectonic processes on Earth and consists of a lithospheric plate descending into the deep mantle. It plays an essential role in the dynamics of global mantle convection and the recycling of geochemical heterogeneities (Goes et al., 2017). The cold subducting slabs are commonly imaged as high-velocity anomalies (HVAs) from seismic tomographic inversions, which suggest that the geometry and sinking rate of the subducting slabs vary considerably, ranging from stagnation in the mantle transition zone (MTZ) to direct penetration into the lower mantle (e.g., Fukao et al., 2001; Hall and Spakman, 2015; Goes et al., 2017; Lu et al., 2019). Materials escaped from the subducted oceanic lithosphere may work as a major source for generating chemical and mineral phase heterogeneities in the mantle (Deuss et al., 2006; Chen et al., 2017; Hao et al., 2019). Extensive geoscientific studies have been conducted beneath the currently active subduction zones, while observational evidence for the tectonics and heterogeneities brought by post-subducted slab segments, which have detached from the surface plates, is relatively scarce (Fukao et al., 2001; Goes et al., 2017).

An oceanic basin named the Proto-South China Sea (PSCS) was proposed to have existed between South China and Borneo in the latest Cretaceous (e.g., Lee and Lawver, 1994; Hall, 2012; Hall and Breitfeld, 2017) and was subsequently eliminated by the southward subduction beneath northern Borneo (Sabah) during the period between the Eocene (33 Ma) and early Miocene (15 Ma, e.g., Taylor and Hayes, 1983; Briais et al., 1993). The slab-pull force associated with the southward subduction was considered as the ultimate driver that broke the South China continental margin and led to the opening of the modern South China Sea (SCS), which is one of the largest marginal seas of the western Pacific Ocean. Thus, Borneo and its adjacent areas are an ideal location to investigate thermal and chemical heterogeneities in the mantle possibly associated with the sinking of the post-subducted slab segments (Fig. 1).

The PSCS subduction was proposed primarily on the basis of surface geological observations and magmatic studies (e.g., Taylor and Hayes, 1983; Hutchison, 1996; Morley, 2002; Hall and Breitfeld, 2017) and is further supported by tomographic images of various slab-like HVAs in the mantle (Tang and Zheng, 2013; Hall and Spakman, 2015; Huang et al., 2015; Zenonos et al., 2019). In addition, a review of strike-slip faults, rift basins and metamorphic core complexes in SE Asia calls for the necessity of including the PSCS subduction for explaining the geological evolution of northern Borneo (Morley, 2002). However, there is little agreement on
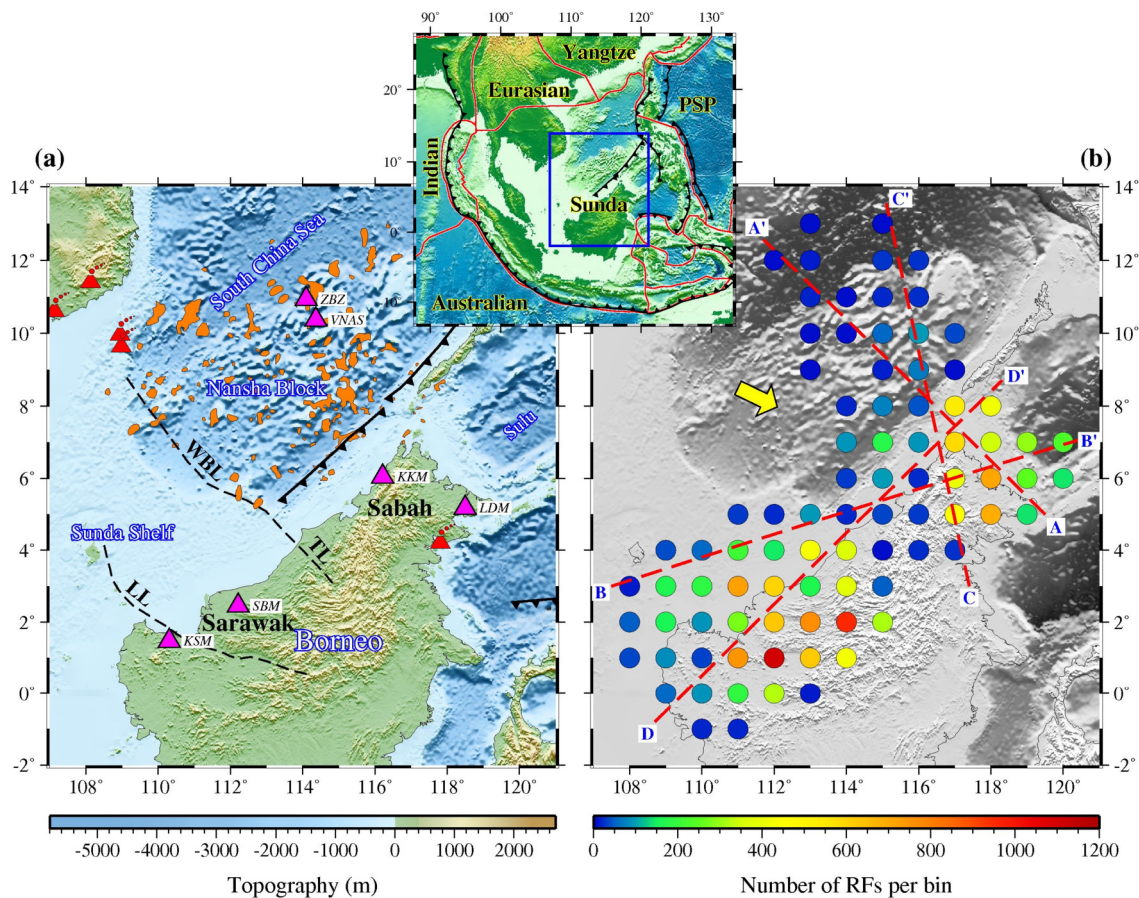
Fig. 1. Tectonic setting and data used in this study. (a) Topographic map showing the distribution of broadband seismic stations (purple triangles). Red triangles represent Cenozoic volcanoes. Orange colored areas display the distribution of the post-spreading basalts (Hui et al., 2016). Solid and dashed lines indicate trench and fault, respectively. LL: Lupar Line; TL: Tinjar Line; WBL: West Baram Line. (b) Number of receiver functions (RFs) for each bin with a radius of 1 degree. Red dashed lines display the locations of cross-sections shown in Fig. 6. Yellow arrow shows the absolute plate motion with a speed of 23 mm/yr based on the NNR-MORVEL56 model (Argus et al., 2011). Insert map depicts the location of the study area highlighted by the blue rectangle. Red and black lines denote plate boundaries and trench, respectively. PSP: Philippine Sea Plate. (For interpretation of the colors in the figure(s), the reader is referred to the web version of this article.)

the current location of the post-subducted PSCS slab segments among previous regional and global seismic tomography models, ranging from residing in the MTZ (e.g., Rangin et al., 1999; Huang et al., 2015; Zenonos et al., 2019) to have dropped into the lower mantle (e.g., Hall and Spakman, 2015). Such discrepancies are mostly due to the sizable (at least 100-200 km) vertical smearing effects and the intrinsic limit of the tomography methods. An alternative collision-driven extrusion model has also been proposed, which advocates that the extrusion of the Indochina Block was mainly responsible for the SCS spreading as a consequence of India indentation into Asia without the involvement of the PSCS (Tapponnier et al., 1982; Replumaz and Tapponnier, 2003). Therefore, the present-day existence and depth extent of the PSCS slab are still a subject of continuing debate, which can be possibly clarified by exploring the MTZ structure.

The MTZ is defined as the portion of the mantle sandwiched between the 410 km (d410) and 660 km (d660) discontinuities, which are revealed to possess positive and negative Clapeyron slopes, respectively, correspondingly leading to thinned MTZ in warm and thickened MTZ in cold regions (Ringwood, 1975; Bina and Helffrich, 1994). The addition of water has a similar effect as decreased temperature (Litasov et al., 2005). In addition, the existence of materials segregated from the subducted slabs can generate additional phase discontinuities above (in the depth range of 250-350 km) or below (about 700-750 km) the MTZ (Zheng et al., 2007; Chen et al., 2017; Hao et al., 2019), which have been proposed to be attributed to phase transitions from coesite to

stishovite and from ilmenite to perovskite, respectively (e.g., Simmons and Gurrola, 2000; Williams and Revenaugh, 2005). Thus, exploring the detailed structure of the multiple discontinuities associated with the MTZ can help decipher both thermal and chemical heterogeneities in the deep mantle.

Previous MTZ studies beneath Borneo and its adjacent areas are quite limited and controversial. A thinned MTZ is found beneath northern Borneo based on P-to-S converted waves recorded by a single station (Saita et al., 2002), while an analysis of SS precursors by employing a depth migration algorithm determines an MTZ that is thickened by at least 20 km in the same region (Dokht et al., 2018). A method of ScS reverberation migration was recently developed and applied to study the MTZ structure in eastern Asia and the western Pacific region, and reveals a thickened MTZ beneath Borneo with a limited spatial resolution due to the large Fresnel zone of the ScS phases (Haugland et al., 2020).

Here, we have conducted a systematic receiver function (RF) study of the MTZ beneath Borneo and the southern SCS based on a non-plane wave common-conversion-point stacking method (Gao and Liu, 2014a) by employing all the available broadband data (Fig. 1). Relative to SS and ScS based methods, the RF technique can help reveal compositional heterogeneities at smaller scale. Our observations present direct and robust evidence for the existence of the PSCS slab and reveal additional discontinuities besides the d410 and d660, which are further determined to be associated with the post-subducted slab segments when combined with mineral experimental and tomographic results. The observations pro-

vide the convincing evidence on the role that the southward PSCS subduction played on the formation and spreading of the SCS.

2. Data and methods

2.1. Data selection and receiver function

Broadband seismic data used in this study were recorded by a total of 6 stations from two sources, including (1) 5 stations with data publicly accessed through the Incorporated Research Institutions for Seismology (IRIS) Data Management Center (DMC), among which 4 permanent stations are situated at the Borneo island with a continuous recording period of 15 years from 2005 to 2020, which offers strong data support for systematically exploring the MTZ structure in detail; (2) station ZBZ deployed by National Marine Environmental Forecasting Center, China with operation time starting from August, 2019, which provides precious new data to greatly enhance coverage and resolution of our dataset for the SCS area. An empirical formula was employed to determine the cut-off magnitude of Mc with the purpose of balancing the quantity and quality of the requested data, which is defined as $Mc = 5.2 + (De - 30)/(180 - 30) - He/700$, where De and He indicate the epicentral distance in degree (ranging from 30° to 100°) and the event depth in kilometer, respectively (Liu and Gao, 2010). All the original seismograms of the selected events were windowed 20 s before and 260 s after the first P wave arrival predicted from the IASP91 Earth model (Kennett and Engdahl, 1991) and were subsequently bandpass filtered by applying a four-pole, two-pass Bessel filter in the frequency band of 0.02-0.2 Hz. We adopted a series of exponential weighting functions with a window width of 60 s centered at the strong PP arrivals to minimize its degenerating effects on the resulting RFs (Gao and Liu, 2014a). The filtered and preprocessed seismograms with a signal-to-noise ratio (SNR) above 4 on the vertical component were converted into radial RFs by deconvolving the vertical from the radial components in the frequency domain with a Gaussian factor of 5.0 and a water-level parameter of 0.03 (Ammon, 1991). The SNR of the vertical component was calculated by the division between the maximum absolute amplitude within 8 s before and 12 s after the theoretical arrival time of the first P wave and the mean absolute amplitude in the time range of 10-20 s before the onset of the predicted arrival. Another SNR-based procedure (Gao and Liu, 2014a) was utilized to select the high-quality RFs, which were then visually checked to reject those without a clear first P wave arrival or with abnormally large arrivals in the P wave coda. In addition, we have also employed a reverberation-removal technique to reduce possible effects from the shallow sedimentary layer (Yu et al., 2015). As a result, there was a total of 5802 RFs (Fig. 1) obtained from 2857 events (Fig. S1) used in this study.

2.2. Moveout correction and stacking

The procedure for moveout correction and stacking of P-to-S converted phase (Pds) arrivals is similar to the traditional common-conversion-point (CCP) method (Dueker and Sheehan, 1997) but was developed under the nonplane wave assumption (Gao and Liu, 2014a). Such an assumption considers the slight difference in ray parameters between the direct P-wave and the Pds, and then improves the accuracy of the predicted Pds travel time, leading to more reliably determined discontinuity depths and sharper arrivals. We computed the locations of the ray piercing points at approximately the middle of the MTZ (535 km) based on the IASP91 Earth model. The study area is evenly divided into overlapping circular bins with a radius of 1°, which is comparable to the radius of the first Fresnel zone of the Pds at the MTZ

depth range, and the distance between the center of nearby bins is also 1°. The time series RFs with their ray piercing point locations falling into a given bin were then moveout corrected and stacked for the depth range of 300-800 km with a vertical interval of 1 km to generate a depth trace by

$$S(d) = \frac{1}{N} \sum_{i=1}^{N} A_i(t_i) \qquad (1)$$

where $S(d)$ is the stacking amplitude at a discontinuity depth of d obtained from a total of N RFs in the bin, and $A_i(t_i)$ is the amplitude of the ith RF at the nonplane wave Pds moveout time (t_i) for the candidate depth d. The way of grouping the RFs at the middle of the MTZ aims to minimize possible bias on the resulting MTZ thickness associated with the lateral upper mantle velocity heterogeneities (Gao and Liu, 2014b). To ensure reliability and spatial coverage, a bin was dropped if N is less than 6. The number of RFs inside each bin ranges from 6 to 1103 with an average of 198 (Fig. 1). The optimal discontinuity depths were initially determined by searching for the maximum stacking amplitude in the depth range of 320-370 km for d350 (350 km discontinuity), 380-440 km for d410, 630-690 km for d660 and 700-760 km for d730 (730 km discontinuity), respectively. We manually checked all the resulting peaks, adjusted some of the searching ranges by considering the spatial consistency and rejected those with weak or ambiguous arrivals. All the final depth traces are plotted based on the increasing depths of the d350, d410, d660 and d730 (Fig. 2), and along each latitudinal cross section with prominent peaks around the depths of the d350, d410, d660 and d730 (Figs. S2-S4). In addition, RFs from each of the stations were individually migrated and stacked to offer a general glance on the data quality by following the same procedures above (Fig. S5). We estimated the mean and standard deviation of the discontinuity depths (Fig. S6) by applying a bootstrap resampling approach (Efron and Tibshirani, 1986) with 50 iterations for each bin, considering a balance between required accuracy, computation times and the number of RFs for each bin. To validate and further confirm the reliability of the observed peaks, we have conducted vespagram analysis using RFs from the entire dataset and three individual subareas of Nansha, Sabah and Sarawak (Fig. 3). The stacked depth series and RF stacking results firstly show that P-to-S conversions from the d410 and d660 are clearly identified and reliably constrained. And most of the stacked positive energy around the depths of 350 km and 730 km generally follow the predicted Pds arrivals of the d350 and d730, indicative of real signals (Fig. 3). On a small portion of the depth series, multiple arrivals in the possible depth ranges of the MTZ discontinuities are observed. The picked arrival for a given discontinuity is determined by considering three factors, including 1) the depth is comparable with that in the neighboring bins; 2) the sense of departure (i.e., uplift or depression) from the globally averaged value is consistent with most of the seismic tomography results in the upper mantle and MTZ; and 3) the arrival on the vespagram is close to the theoretical arrival (Fig. 3). As demonstrated below, the main conclusions of the study remain virtually the same even if all the bins with multiple arrivals were excluded.

2.3. Velocity correction of mantle discontinuity depths

The resulting discontinuity depths are apparent instead of true depths due to the employment of 1-D IASP91 Earth model for moveout correction and time-depth conversion. In order to determine the true depths for each discontinuity, we need well-determined both Vp and Vs velocity models with sufficient lateral and vertical resolutions for the layers above the discontinuities by following a formula below (Gao and Liu, 2014a):
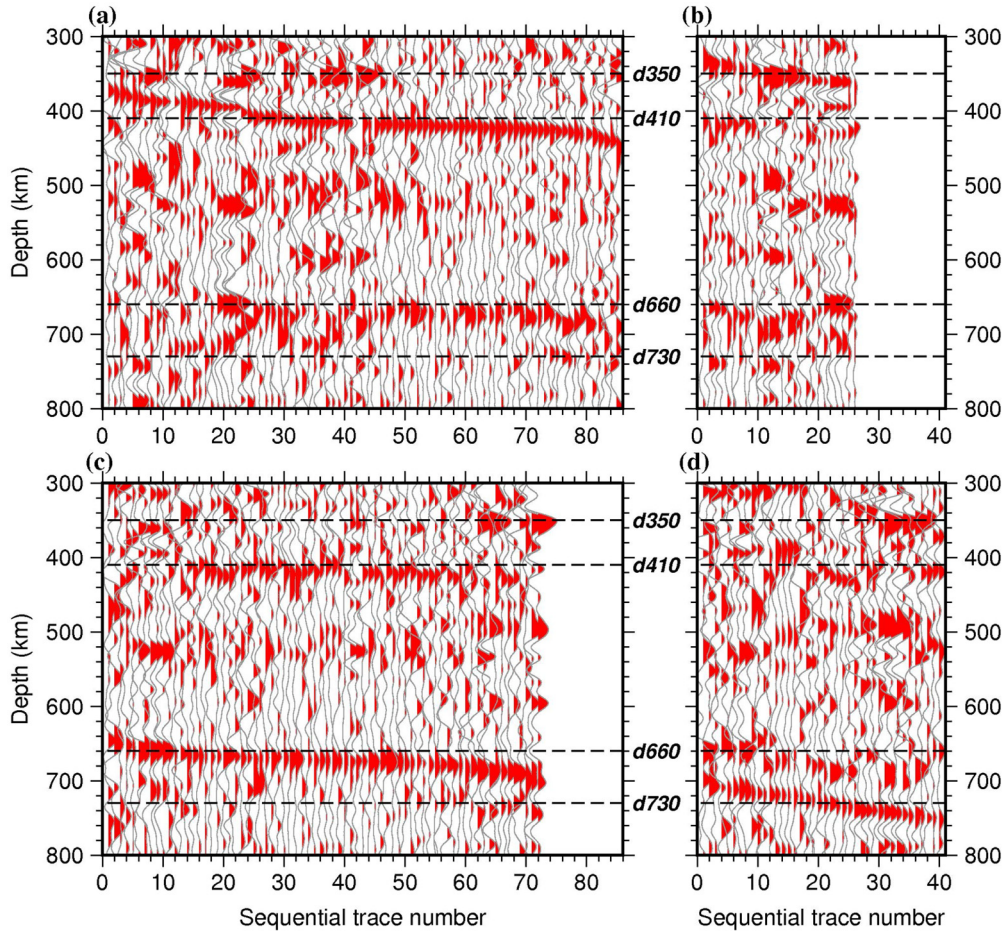
Fig. 2. Display of all the stacking RF traces. (a) Binned RFs are sequentially presented according to the increasing depth of the 410 km discontinuity (d410). (b-d) Same as (a) but for the 350 km (d350), 660 km (d660) and 730 km (d730) discontinuities, respectively.

$$D_T = \frac{(V_{S0} + \delta V_S) \times (V_{P0} + \delta V_P)}{V_{P0} + \delta V_P - V_{S0} - \delta V_S} \times \frac{V_{P0} - V_{S0}}{V_{P0} \times V_{S0}} D_A \qquad (2)$$

where D_A and D_T are the resulting apparent and velocity-corrected true discontinuity depths, respectively, $(V_{P0}, \delta V_P)$ and $(V_{S0}, \delta V_S)$ correspond to the mean velocity in the standard Earth model and absolute velocity anomalies in the layer for P- and S-wave. We have employed a recent global (Lu et al., 2019) and one regional (Zenonos et al., 2019) tomography models (including both Vp and Vs anomalies) to conduct velocity corrections of the resulting discontinuity depths based on equation (2).

3. Results and discussion

3.1. Post-subducted slab segments of the Proto-South China Sea in the MTZ

There is a total of 86 bins with identifiable either d410 or d660 phases, among which 85 bins present well-determined d410 arrivals, 72 bins have reliable d660 peaks, and 71 bins possess both (Fig. 2). The observed apparent depths of the d410 and d660 are spatially heterogeneous and vary from 371 km to 447 km with an average of 411±17 km and from 644 km to 701 km with a mean value of 671±11 km, respectively (Fig. 4 and Table S1). Significant variations of the resulting MTZ thickness are also revealed to range from 220 km to 322 km with a mean of 260±16 km, which is generally consistent with results from analysis of SS precursor (Dokht et al., 2018) and ScS reverberations (Haugland et al., 2020). Most of the large MTZ thickness measurements are situated at Sabah and

its surrounding areas, and have a mean value of 270±17 km calculated from a total of 33 bins (Fig. 4), which is significantly greater than the theoretical value of 250 km from the IASP91 Earth model. The cross-correlation coefficient (XCC) of 0.32 between the apparent depths of the d410 and d660 (Fig. 4) is substantially lower than the value of 0.84 for the contiguous United States (Gao and Liu, 2014b). In addition to the d410 and d660, spatially coherent arrivals around the depths of 350 km (d350) and 730 km (d730) are also observed (Figs. 5 and 6).

To the first order, prominent MTZ thickening is mostly revealed beneath Sabah and the southern margin of the SCS (the Nansha Block area) based on the resulting apparent and velocity-corrected observations (Fig. 4), and its distribution is reasonably consistent with that of the HVAs around the MTZ depths (Fig. 6) imaged by seismic tomography (Rangin et al., 1999; Huang et al., 2015; Lu et al., 2019). These measurements of thickened MTZ provide direct and independent evidence for the existence of slab segments (commonly characterized as cold features) in the MTZ beneath northern Borneo and the Nansha Block.

Because it has been estimated that the period of a slab stagnation in the MTZ is unlikely to exceed 60 Ma (Goes et al., 2017), the revealed slab segments are not likely originated from older subductions in the Cretaceous (older than 66 Ma). Thus, the slab segments are more likely related to a recently terminated subduction in the Cenozoic. Various models of plate reconstruction (Lee and Lawver, 1994; Hall, 2012; Wu and Suppe, 2018) reveal a Mesozoic PSCS existing between the Nansha Block and northern Borneo (Fig. 5), which was subsequently eliminated by the southward subduction beneath Borneo between the Oligocene and
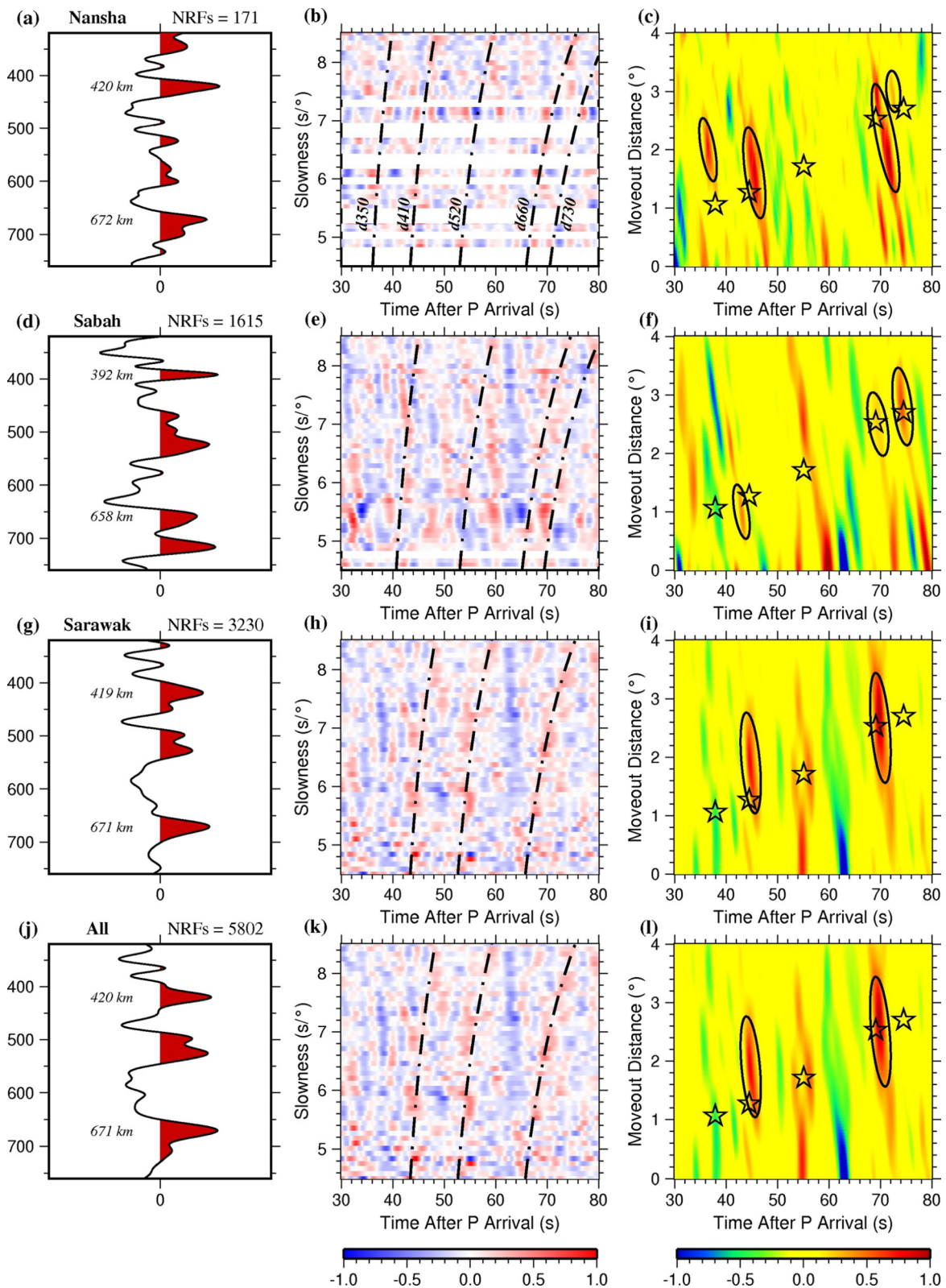
Fig. 3. Vespagram analysis for three subareas of Nansha (a, b, c), Sabah (d, e, f) and Sarawak (g, h, i), and the entire dataset (j, k, l). (a, d, g, j) Resulting depth series by stacking RFs from each corresponding area. (b, e, h, k) Stacked and normalized RFs in slowness bins. Hachured lines delineate the arrivals of the P-to-S converted phases at the d350, d410, d520, d660 and d730. (c, f, i, l) RF stacking results by referring to a slowness of 6.5 s per degree. The stars and ellipses mark the predicted and observed arrivals, respectively.

Middle Miocene (Taylor and Hayes, 1983; Briais et al., 1993). The involvement of the PSCS can better explain the Cenozoic geological history of Borneo than most other models (Hutchison, 1996; Hall and Breitfeld, 2017). The continuously southward subduction

of the PSCS and its cessation put northern Borneo in an accretionary setting (Rangin et al., 1990; Morley, 2002; Cullen, 2014) and its crust is recently determined to possess an abnormal thickness of 39.1 km which is about 15 km thicker than that of Sarawak
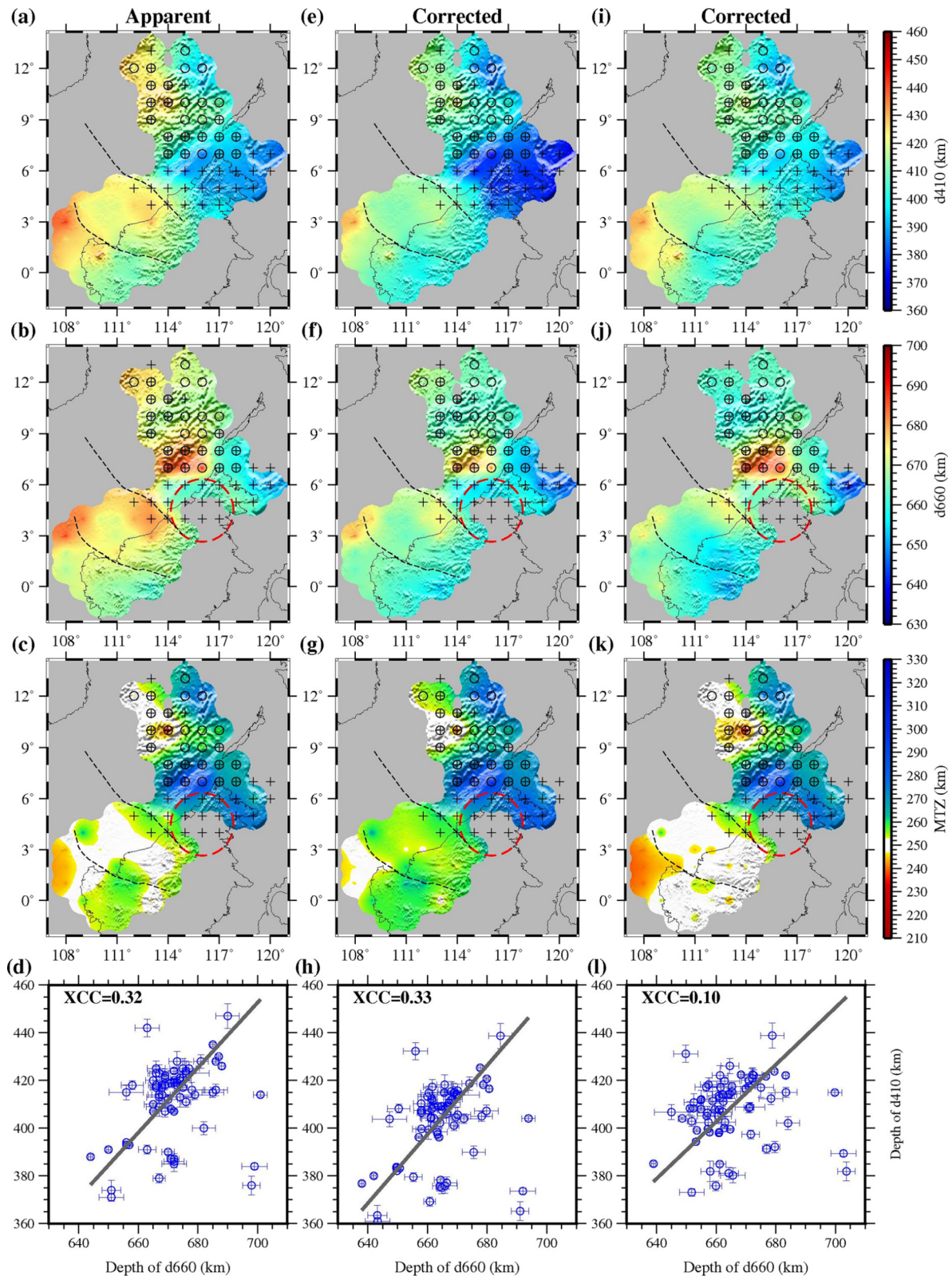
Fig. 4. Resulting mantle transition zone (MTZ) discontinuity depths and thickness. (a-c) Spatial distributions of the observed apparent depths of the d410 and the d660, and MTZ thickness measurements. Circles and pluses represent bins with well-defined arrivals of the d350 and the d730, respectively. Red dashed circles highlight the area where the d660 is rarely identified while the d730 is clearly observed. (d) Correlation plot between the apparent depths of the d410 and d660. The thick gray line indicates the optimal fitting line with a cross correlation coefficient (XCC) of 0.32. (e-h) and (i-l) are same as (a-d) but for velocity-corrected results from a global (Lu et al., 2019) and a regional (Zenonos et al., 2019) tomography models, respectively.

(Gao et al., 2020). Analysis of Rayleigh wave dispersion curves reveals a SE dipping HVA beneath northern Borneo, which is interpreted as a segment of the PSCS slab (Tang and Zheng, 2013)

and is further confirmed by a recent body-wave tomography inversion (Zenonos et al., 2019). New shear wave splitting measurements also favor the existence of a detached slab beneath Sabah
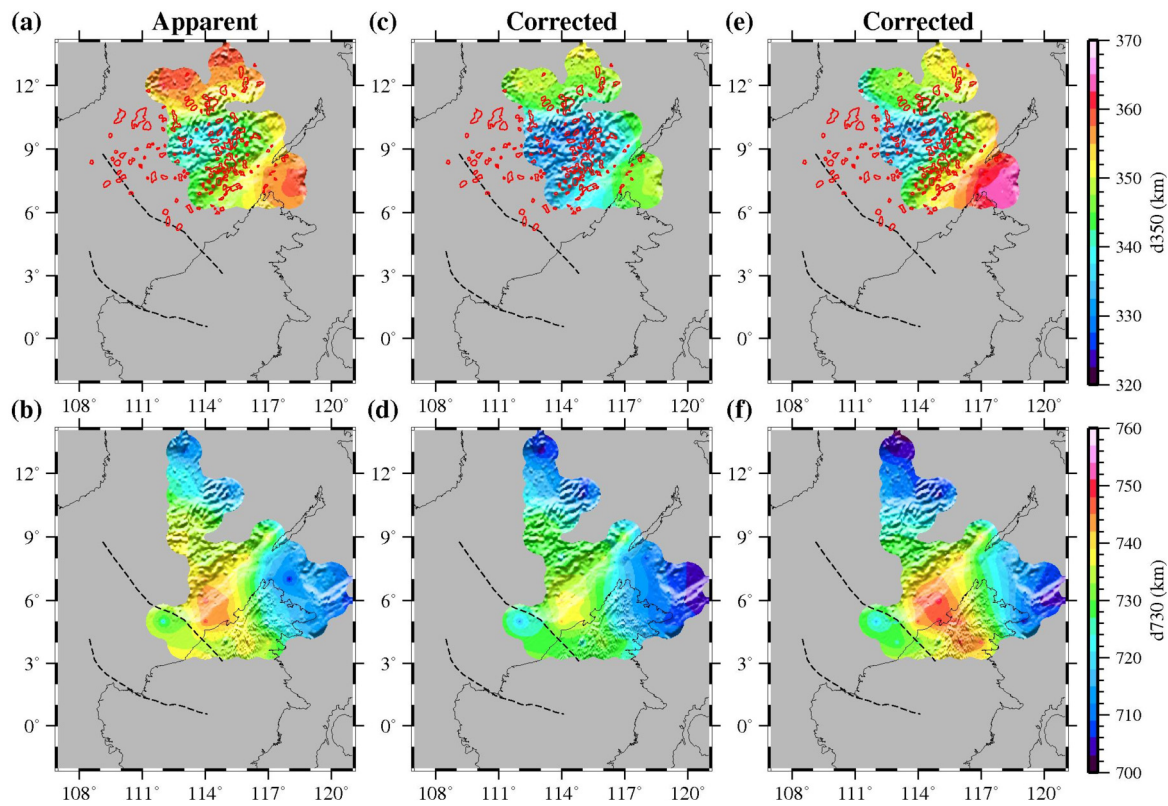
Fig. 5. Apparent and velocity-corrected depths of the d350 and d730. (a-b) Contour maps of the resulting apparent depths of the d350 and d730, respectively. (c-d) and (e-f) correspond to the velocity-corrected measurements from a global (Lu et al., 2019) and one regional (Zenonos et al., 2019) tomography models.

where the dominantly absolute plate motion driven mantle flow is significantly modified and deflected (Song et al., 2021). Thus, our observations, when combined with other geophysical and geological evidence, confirm the existence of the PSCS subduction beneath Borneo. They also indicate that a significant portion of the post-subducted slab segments currently situate in the MTZ, having not fully sunk into the lower mantle (Fig. 7).

The oceanic plate is extensively hydrated, and its stored water can be released by dehydration from the PSCS slab segments in and around the MTZ, which would contribute to water-induced MTZ thickening in addition to that induced by the cold temperature (Litasov et al., 2005). Experimental (Inoue et al., 1998) and observational (Deuss and Woodhouse, 2001; Van der Meijde et al., 2003; Yu et al., 2020) studies indicate that an increased water content in the MTZ would reduce the stacking amplitude of the d410 and make the 520 km discontinuity (d520, usually representing the phase transition from wadsleyite to ringwoodite) easier to be detected and split, which are all revealed in the resulting RF traces (Figs. 6 and S2-S4). The sinking of the post-subducted PSCS slab could have promoted the development of mantle upwelling along its edge (Fig. 7), which can explain the observed slight MTZ thinning near Sarawak (Fig. 4). Similar mechanisms are also revealed beneath the adjacent Indochina Peninsula (Yu et al., 2017). Part of the dehydrated water or segregated slab materials may have been carried to the surface by the mantle upwelling, giving rise to the adakite-dacite type intrusion and volcanic activities observed beneath Sarawak (Khan et al., 2017; Breitfeld et al., 2019; Gao et al., 2020).

3.2. Contribution of slab dehydration to post-spreading volcanism of the southern SCS

The d350 is observed at 26 bins mostly located in the Nansha Block where a thickened MTZ is observed (Figs. 5 and 6, Table S2). This discontinuity possesses a stacking amplitude that is comparable to that of the d410, and has an apparent depth ranging from 332 km to 364 km and a mean depth of 350±10 km. Intermittent seismic discontinuity at 250-350 km is usually named the X-discontinuity (Revenaugh and Jordan, 1991). Experimental studies indicate that mineral phase transition from coesite to stishovite offers a plausible explanation for this discontinuity (Williams and Revenaugh, 2005; Chen et al., 2017). Eclogitic or hydrated materials segregated from the residue of ancient subduction can provide geochemical heterogeneities for the development of the seismically observable X-discontinuity (Williams and Revenaugh, 2005). The topography of the d350 has a generally SE-dipping shallow angle based on the velocity-corrected results (Fig. 5). This observation, together with the spatial correspondence between the area with observable d350 and thickened MTZ, suggests that the d350 can be attributed to the post-subducted slab segments of the PSCS, similar to those observed at the Tonga subduction (Zheng et al., 2007). This is consistent with the observation that the vertical distribution of the d350 closely follows the geometry of the remnant slab.

Since the cessation of the SCS spreading, widespread magmatic activities (e.g., Hui et al., 2016; Song et al., 2017) have occurred in the continental slope regions and the central SCS basin including its southern margin (Figs. 1 and 5). Sills, dykes, and plutonic materials with an age of middle Miocene to Pleistocene are observed in the Nansha Block (Schlüter et al., 1996; Song et al., 2017). Analysis of multi-channel seismic and gravity data reveals volcanic intrusion into the crust around the Taiping island (Chang et al., 2017), which is further supported by the recently observed high Vp/Vs ratio from RF investigation (Gao et al., 2020). However, the mechanism of post-spreading volcanism remains enigmatic and several models have been proposed including mantle upwelling from the Hainan mantle plume (Xu et al., 2012; Chang et al., 2017) and extension triggered by the subsidence of the cooling SCS lithosphere (Song et al., 2017). The revealed d350 beneath the Nansha Block
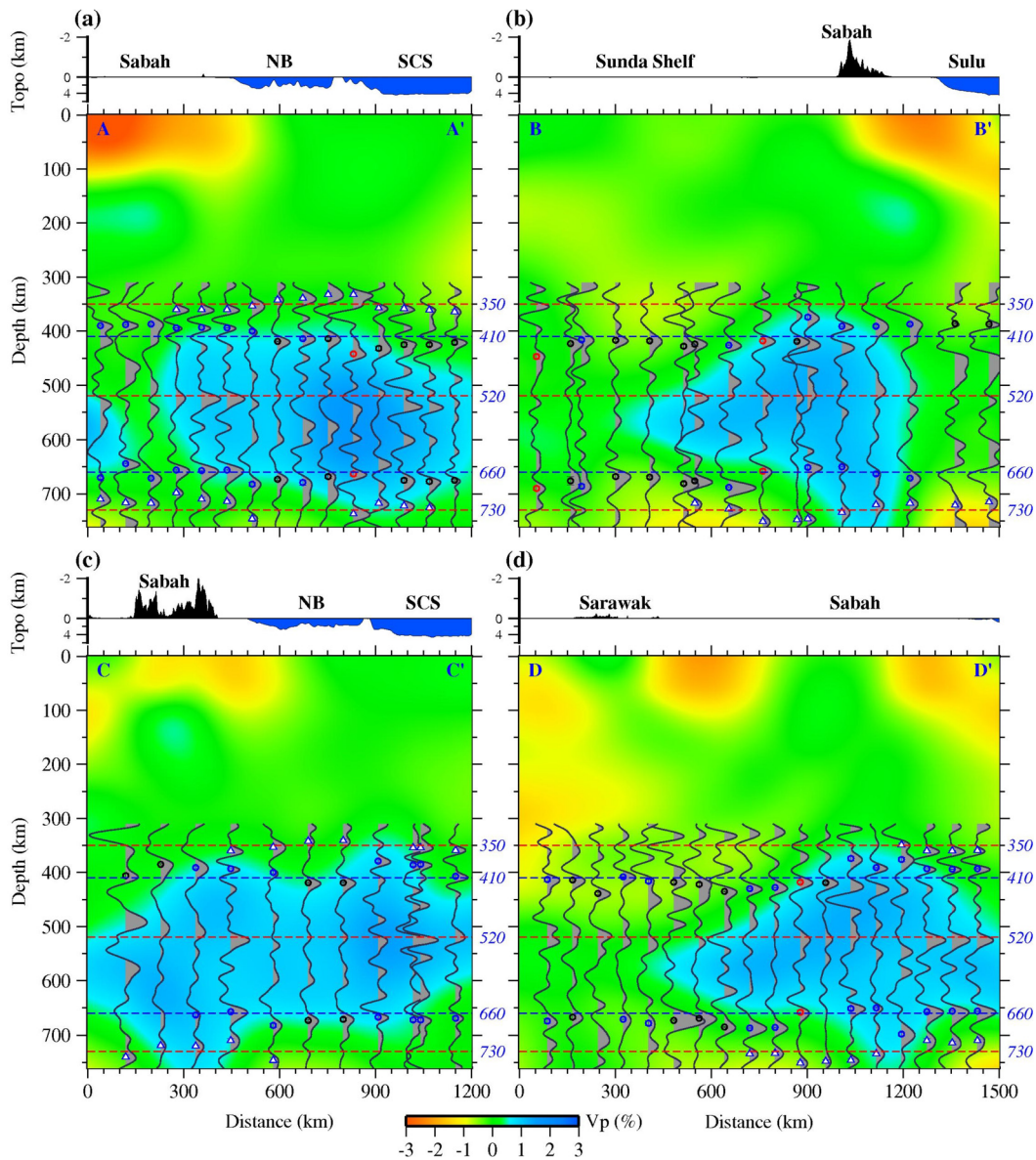
Fig. 6. Vertical display of RF traces and velocity anomalies. The upper panels present cross sections of the elevations and the lower ones show the resulting stacking RF traces and P-wave tomography (Huang et al., 2015) along the four profiles shown in Fig. 1b. Circles and white triangles indicate well-determined peaks of the d410-d660 and d350-d730, respectively. Red and blue circles denote measurements with their MTZ thickness at least 5 km less and larger than 250 km, respectively. NB: Nansha Block; SCS: South China Sea.

may indicate that melting from the subducted slab segments is a viable source for the post-spreading magmatism. Shallow volcanism can be instigated by fluid-assisted decompression melting from convective dehydration of the subducted slab segments (Fig. 7b), which has been proposed to explain intraplate volcanism based on numerical modeling analysis (Long et al., 2019). The water content in the slab is globally modeled to have dehydrated by 66% when reaching 240 km depth (van Keken et al., 2011). The Nansha Block (Fig. 1) is determined to move southeastwards (by 116 degrees counting clockwise from north) at a speed of about 23 mm/yr based on the NNR-MORVEL56 model (Argus et al., 2011), which can explain the observation that the subducted slab segments are currently situated beneath the Nansha Block (Fig. 5). Assuming a constant plate motion velocity since the termination of the Proto-SCS subduction at about 15 Ma, the Nansha Block would have moved 345 km toward the southeast, which agrees well with the current position of the revealed slab segments. The shallow asthenosphere under the Nansha Block is characterized as

having low-velocity (Tang and Zheng, 2013) and high-temperature (Dong et al., 2019) anomalies, which can be possibly attributed to the deep ongoing dehydration melting from the revealed slab segments (Fig. 7). The sinking rate of the post-subducted slab segments is estimated to be about 2 cm/yr, which is comparable to the average value of 1-3 cm/yr for the Tethyan subducted slabs (e.g., Van der Voo et al., 1999; Zahirovic et al., 2012).

3.3. Penetration of slab materials into the lower mantle

The d730 just below the MTZ is systematically observed from a total of 40 bins and its apparent depth is determined to range from 698 km to 751 km with an average of 728±15 km. Significant depressions of the d730 are mostly situated around the Sabah area (Fig. 5). Such a discontinuity is possibly induced by compositional heterogeneities associated with the revealed slab segments. Multiple seismic discontinuities below the MTZ have been extensively detected beneath areas where cold thermal anomalies associated
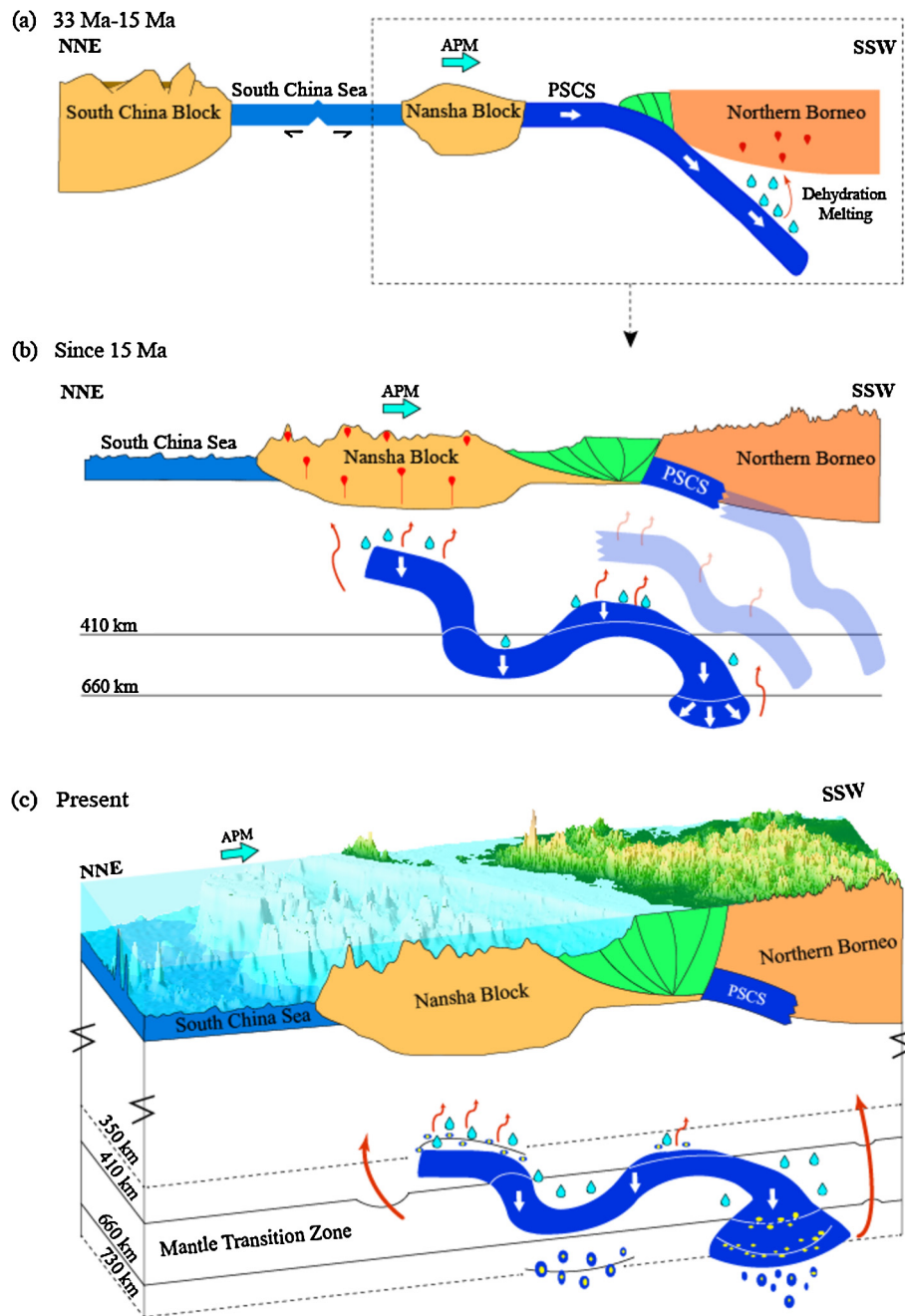
Fig. 7. Schematic cartoon for tectonic evolution of the Proto-South China Sea (PSCS). APM: Absolute Plate Motion. The cyan drops denote dehydrated water. Red arrows indicate dehydration melting or mantle upwelling associated with the sinking of the PSCS slab. Yellow dots in (c) represent segregated materials from the post-subducted slab. Shadowed slabs are plotted in a smaller scale and display the dropping processes. The green area represents accretionary prism.

with subducted or foundered lithospheric segments exist (e.g., Simmons and Gurrola, 2000; Ai et al., 2003; Deuss et al., 2006; Tibi et al., 2006; Yu et al., 2020) and are ascribed to a phase transition from ilmenite to perovskite under a pyrolite mantle composition (Ai et al., 2003; Deuss et al., 2006; Tibi et al., 2006). In addition, the decomposition of pyrope into bridgmanite and corundum under a lower temperature environment is recently reported to be a plausible cause for the discontinuity at about 700-750 km based on mineralogical experiments (Hao et al., 2019). The robust d730 combined with the imaged HVAs and observed MTZ thickening directly above it offer clues that the post-subducted slab segments of the PSCS may have partly penetrated the MTZ into the lower mantle and generated compositional heterogeneities at the uppermost lower mantle (Fig. 5).

The sinking PSCS slab would fold, thicken, and eventually travel through the MTZ into the lower mantle driven by the Rayleigh-Tayler type gravitational instability (Goes et al., 2017). The relatively young age of the Mesozoic PSCS during its southward subduction makes the subducted slab easier to sink into the lower mantle (Goes et al., 2017; Agrusta et al., 2017). Due to the increased viscosity, the uppermost lower mantle may trap part of the sinking post-subducted slab segments and promote the development of a slab reservoir at the base of the MTZ (Fukao et al., 2001), which has been widely observed for the ancient slab remnants of the Farallon plate under North America (Sigloch and Mihalynuk, 2013) and the Tethys plate beneath the Tibetan Plateau (Fukao et al., 2001). Crustal materials segregated from the penetrated slab are neutrally buoyant and would bring rheological and

compositional heterogeneities, contributing to the formation of the d730 (Deuss et al., 2006; Hao et al., 2019). One circular area is highlighted at southern Sabah (Fig. 4) where the d660 is too weak to be observed while the signal of the d730 is quite strong (Fig. 5). Such a feature may be attributed to the slab penetration, which would possibly decrease the velocity contrast across the d660. The distributions of the observed d350, d730 and MTZ thickening together generally depict the lateral extent of the subducted PSCS to the west and are mostly located east of the Tinjar-West Baram Line, which represents a dextral transform fault and is believed to be the western boundary of the PSCS (Morley, 2002; Cullen, 2014; Hall and Breitfeld, 2017). A similar geometry of the PSCS is also revealed from a slab-based plate reconstruction (Wu and Suppe, 2018).

4. Conclusions

In this study, we have employed the receiver function analysis of all the available seismic broadband data to systematically explore the MTZ structure beneath Borneo and the southern South China Sea (SCS). Significant MTZ thickening with an average of 270±17 km is revealed at Sabah (northern Borneo) and the southern SCS, and provides so far the most convincing evidence on the existence of slab segments in the MTZ, which is further determined to be possibly originated from the post-subducted Proto-SCS. Additional mantle discontinuities above and below the MTZ at the depths of 350 km (d350) and 730 km (d730) are observed at areas of MTZ thickening and can be attributed to the involvement of heterogeneous materials segregated from the post-subducted Proto-SCS slab segments. Dehydration melting from the sinking slab segments may offer a viable source and contribute to the widespread post-spreading magmatism of the southern SCS. Our observations indicate that the post-subducted slab segments play a significant role in developing layered mantle heterogeneities, and therefore have broad implications for better understanding the evolution of other ancient slabs such as the Farallon and Tethys plates and the roles that they play in modulating crustal and mantle dynamic processes.

CRediT authorship contribution statement

Youqiang Yu: Conceptualization, Methodology, Writing – original draft. **Zhiguo Xu:** Data curation. **Stephen S. Gao:** Writing – review & editing. **Kelly H. Liu:** Writing – review & editing. **Jia Gao:** Resources, Visualization.

Declaration of competing interest

The authors declare that they have no known competing financial interests or personal relationships that could have appeared to influence the work reported in this paper.

References

Agrusta, R., Goes, S., van Hunen, J., 2017. Subducting-slab transition-zone interaction: stagnation, penetration and mode switches. Earth Planet. Sci. Lett. 464, 10–23. https://doi.org/10.1016/j.epsl.2017.02.005.

Ai, Y., Zheng, T., Xu, W., He, Y., Dong, D., 2003. A complex 660 km discontinuity beneath northeast China. Earth Planet. Sci. Lett. 212 (1–2), 63–71. https://doi.org/10.1016/S0012-821X(03)00266-8.

Ammon, C.J., 1991. The isolation of receiver effects from teleseismic P waveforms. Bull. Seismol. Soc. Am. 81, 2504–2510.

Argus, D.F., Gordon, R.G., DeMets, C., 2011. Geologically current motion of 56 plates relative to the no-net-rotation reference frame. Geochem. Geophys. Geosyst. 12, Q11001. https://doi.org/10.1029/2011GC003751.

Bina, C.R., Helffrich, G., 1994. Phase transition Clapeyron slopes and transition zone seismic discontinuity topography. J. Geophys. Res., Solid Earth 99 (B8), 15853–15860. https://doi.org/10.1029/94JB00462.

Breitfeld, H.T., Macpherson, C., Hall, R., Thirlwall, M., Ottley, C.J., Hennig-Breitfeld, J., 2019. Adakites without a slab: remelting of hydrous basalt in the crust and shallow mantle of Borneo to produce the Miocene Sintang Suite and Bau Suite magmatism of West Sarawak. Lithos 344, 100–121. https://doi.org/10.1016/j.lithos.2019.06.016.

Briais, A., Patriat, P., Tapponnier, P., 1993. Updated interpretation of magnetic anomalies and seafloor spreading stages in the South China Sea: implications for the Tertiary tectonics of Southeast Asia. J. Geophys. Res., Solid Earth 98 (B4), 6299–6328. https://doi.org/10.1029/92JB02280.

Chang, J.H., Hsieh, H.H., Mirza, A., Chang, S.P., Hsu, H.H., Liu, C.S., Su, C.C., Chiu, S.D., Ma, Y.F., Chiu, Y.H., Hung, H.T., Lin, Y.C., Hung, H.T., 2017. Crustal structure north of the Taiping Island (Itu Aba Island), southern margin of the South China Sea. J. Asian Earth Sci. 142, 119–133. https://doi.org/10.1016/j.jseaes.2016.08.005.

Chen, T., Liebermann, R.C., Zou, Y., Li, Y., Qi, X., Li, B., 2017. Tracking silica in Earth's upper mantle using new sound velocity data for coesite to 5.8 GPa and 1073 K. Geophys. Res. Lett. 44 (15), 7757–7765. https://doi.org/10.1002/2017GL073950.

Cullen, A., 2014. Reprint of: nature and significance of the West Baram and Tinjar Lines, NW Borneo. Mar. Pet. Geol. 58, 674–686. https://doi.org/10.1016/j.marpetgeo.2014.01.009.

Deuss, A., Woodhouse, J., 2001. Seismic observations of splitting of the mid-transition zone discontinuity in Earth's mantle. Science 294 (5541), 354–357. https://doi.org/10.1126/science.1063524.

Deuss, A., Redfern, S.A., Chambers, K., Woodhouse, J.H., 2006. The nature of the 660-kilometer discontinuity in Earth's mantle from global seismic observations of PP precursors. Science 311 (5758), 198–201. https://doi.org/10.1126/science.1120020.

Dokht, R.M., Gu, Y.J., Sacchi, M.D., 2018. Migration imaging of the Java subduction zones. J. Geophys. Res., Solid Earth 123 (2), 1540–1558. https://doi.org/10.1002/2017JB014524.

Dong, M., Zhang, J., Wu, S.G., Wang, B.Y., Ai, Y.F., 2019. Cooling of the lithosphere beneath the Nansha Block, South China Sea. J. Asian Earth Sci. 171, 169–177. https://doi.org/10.1016/j.jseaes.2018.06.007.

Dueker, K.G., Sheehan, A.F., 1997. Mantle discontinuity structure from midpoint stacks of converted P to S waves across the Yellowstone hotspot track. J. Geophys. Res., Solid Earth 102 (B4), 8313–8327. https://doi.org/10.1029/96JB03857.

Efron, B., Tibshirani, R., 1986. Bootstrap methods for standard errors, confidence intervals, and other measures of statistical accuracy. Stat. Sci. 1, 54–75. https://projecteuclid.org/euclid.ss/1177013815.

Fukao, Y., Widiyantoro, S., Obayashi, M., 2001. Stagnant slabs in the upper and lower mantle transition region. Rev. Geophys. 39 (3), 291–323. https://doi.org/10.1029/1999RG000068.

Gao, J., Yu, Y., Song, W., Gao, S.S., Liu, K.H., 2020. Crustal modifications beneath the central Sunda plate associated with the Indo-Australian subduction and the evolution of the South China Sea. Phys. Earth Planet. Inter. 306, 106539. https://doi.org/10.1016/j.pepi.2020.106539.

Gao, S.S., Liu, K.H., 2014a. Imaging mantle discontinuities using multiply-reflected P-to-S conversions. Earth Planet. Sci. Lett. 402, 99–106. https://doi.org/10.1016/j.epsl.2013.08.025.

Gao, S.S., Liu, K.H., 2014b. Mantle transition zone discontinuities beneath the contiguous United States. J. Geophys. Res., Solid Earth 119 (8), 6452–6468. https://doi.org/10.1002/2014JB011253.

Goes, S., Agrusta, R., van Hunen, J., Garel, F., 2017. Subduction-transition zone interaction: a review. Geosphere 13 (3), 644–664. https://doi.org/10.1130/GES01476.1.

Hall, R., 2012. Late Jurassic–Cenozoic reconstructions of the Indonesian region and the Indian Ocean. Tectonophysics 570–571 (11), 1–41. https://doi.org/10.1016/j.tecto.2012.04.021.

Hall, R., Breitfeld, H.T., 2017. Nature and demise of the Proto-South China Sea. Bull. Geol. Soc. Malays. 63, 61–76. https://doi.org/10.7186/bgsm63201703.

Hall, R., Spakman, W., 2015. Mantle structure and tectonic history of SE Asia. Tectonophysics 658, 14–45. https://doi.org/10.1016/j.tecto.2015.07.003.

Hao, S., Wang, W., Qian, W., Wu, Z., 2019. Elasticity of akimotoite under the mantle conditions: implications for multiple discontinuities and seismic anisotropies at the depth of ∼ 600–750 km in subduction zones. Earth Planet. Sci. Lett. 528, 115830. https://doi.org/10.1016/j.epsl.2019.115830.

Haugland, S.M., Ritsema, J., Sun, D., Trampert, J., Koroni, M., 2020. Common reflection point mapping of the mantle transition zone using recorded and 3-D synthetic ScS reverberations. Geophys. J. Int. 220 (1), 724–736. https://doi.org/10.1093/gji/ggz467.

Huang, Z., Zhao, D., Wang, L., 2015. P wave tomography and anisotropy beneath Southeast Asia: insight into mantle dynamics. J. Geophys. Res., Solid Earth 120 (7), 5154–5174. https://doi.org/10.1002/2015JB012098.

Hui, G., Li, S., Li, X., Guo, L., Suo, Y., Somerville, I.D., Zhao, S., Hu, M., Lan, H., Zhang, J., 2016. Temporal and spatial distribution of Cenozoic igneous rocks in the South China Sea and its adjacent regions: implications for tectono-magmatic evolution. Geol. J. 51, 429–447. https://doi.org/10.1002/gj.2801.

Hutchison, C.S., 1996. The 'Rajang accretionary prism' and 'Lupar Line' problem of Borneo. Geol. Soc. (Lond.) Spec. Publ. 106 (1), 247–261. https://doi.org/10.1144/GSL.SP.1996.106.01.16.

Inoue, T., Weidner, D.J., Northrup, P.A., Parise, J.B., 1998. Elastic properties of hydrous ringwoodite (γ-phase) in Mg2SiO4. Earth Planet. Sci. Lett. 160 (1–2), 107–113. https://doi.org/10.1016/S0012-821X(98)00077-6.

Kennett, B.L.N., Engdahl, E.R., 1991. Traveltimes for global earthquake location and phase identification. Geophys. J. Int. 105 (2), 429–465. https://doi.org/10.1111/j.1365-246X.1991.tb06724.x.

Khan, A.A., Abdullah, W.H., Hassan, M.H., Iskandar, K., 2017. Tectonics and sedimentation of SW Sarawak basin, Malaysia, NW Borneo. J. Geol. Soc. India 89 (2), 197–208. https://doi.org/10.1007/s12594-017-0584-0.

Lee, T.Y., Lawver, L.A., 1994. Cenozoic plate reconstruction of the South China Sea region. Tectonophysics 235 (1–2), 149–180. https://doi.org/10.1016/0040-1951(94)90022-1.

Litasov, K.D., Ohtani, E., Sano, A., Suzuki, A., Funakoshi, K., 2005. Wet subduction versus cold subduction. Geophys. Res. Lett. 32 (13), L13312. https://doi.org/10.1029/2005GL022921.

Liu, K.H., Gao, S.S., 2010. Spatial variations of crustal characteristics beneath the Hoggar swell, Algeria, revealed by systematic analyses of receiver functions from a single seismic station. Geochem. Geophys. Geosyst. 11, Q08011. https://doi.org/10.1029/2010GC003091.

Long, X., Ballmer, M.D., Córdoba, A.M.C., Li, C.F., 2019. Mantle melting and intraplate volcanism due to self-buoyant hydrous upwellings from the stagnant slab that are conveyed by small-scale convection. Geochem. Geophys. Geosyst. 20 (11), 4972–4997. https://doi.org/10.1029/2019GC008591.

Lu, C., Grand, S.P., Lai, H., Garnero, E.J., 2019. TX2019slab: a new P and S tomography model incorporating subducting slabs. J. Geophys. Res., Solid Earth 124 (11), 11549–11567. https://doi.org/10.1029/2019JB017448.

Morley, C.K., 2002. A tectonic model for the Tertiary evolution of strike–slip faults and rift basins in SE Asia. Tectonophysics 347 (4), 189–215. https://doi.org/10.1016/S0040-1951(02)00061-6.

Rangin, C., Bellon, H., Benard, F., Letouzey, J., Muller, C., Sanudin, T., 1990. Neogene arc-continent collision in Sabah, northern Borneo (Malaysia). Tectonophysics 183 (1–4), 305–319. https://doi.org/10.1016/0040-1951(90)90423-6.

Rangin, C., Spakman, W., Pubellier, M., Bijwaard, H., 1999. Tomographic and geological constraints on subduction along the eastern Sundaland continental margin (South-East Asia). Bull. Soc. Géol. Fr. 170 (6), 775–788.

Replumaz, A., Tapponnier, P., 2003. Reconstruction of the deformed collision zone between India and Asia by backward motion of lithospheric blocks. J. Geophys. Res. 108, 2285. https://doi.org/10.1029/2001JB000661.

Revenaugh, J., Jordan, T.H., 1991. Mantle layering from ScS reverberations: 3. The upper mantle. J. Geophys. Res., Solid Earth 96 (B12), 19781–19810. https://doi.org/10.1029/91JB01487.

Ringwood, A.E., 1975. Composition and Petrology of the Earth's Mantle. McGraw-Hill, New York. 672 pp.

Saita, T., Suetsugu, D., Ohtaki, T., Takenaka, H., Kanjo, K., Purwana, I., 2002. Transition zone thickness beneath Indonesia as inferred using the receiver function method for data from the JISNET regional broadband seismic network. Geophys. Res. Lett. 29 (7), 19-1. https://doi.org/10.1029/2001GL013629.

Schlüter, H.U., Hinz, K., Block, M., 1996. Tectono-stratigraphic terranes and detachment faulting of the South China Sea and Sulu Sea. Mar. Geol. 130 (1–2), 39–78. https://doi.org/10.1016/0025-3227(95)00137-9.

Sigloch, K., Mihalynuk, M.G., 2013. Intra-oceanic subduction shaped the assembly of Cordilleran North America. Nature 496, 50–56. https://doi.org/10.1038/nature12019.

Simmons, N.A., Gurrola, H., 2000. Multiple seismic discontinuities near the base of the transition zone in the Earth's mantle. Nature 405 (6786), 559–562. https://doi.org/10.1038/35014589.

Song, W., Yu, Y., Gao, S.S., Liu, K.H., Fu, Y., 2021. Seismic anisotropy and mantle deformation beneath the central Sunda plate. J. Geophys. Res., Solid Earth 126, e2020JB021259. https://doi.org/10.1029/2020JB021259.

Song, X., Li, C.F., Yao, Y., Shi, H., 2017. Magmatism in the evolution of the South China Sea: geophysical characterization. Mar. Geol. 394, 4–15. https://doi.org/10.1016/j.margeo.2017.07.021.

Tang, Q., Zheng, C., 2013. Crust and upper mantle structure and its tectonic implications in the South China Sea and adjacent regions. J. Asian Earth Sci. 62, 510–525. https://doi.org/10.1016/j.jseaes.2012.10.037.

Tapponnier, P., Peltzer, G.L.D.A.Y., Le Dain, A.Y., Armijo, R., Cobbold, P., 1982. Propagating extrusion tectonics in Asia: new insights from simple experiments with plasticine. Geology 10 (12), 611–616. https://doi.org/10.1130/0091-7613(1982)10<611:PETIAN>2.0.CO;2.

Taylor, B., Hayes, D.E., 1983. Origin and history of the South China Sea basin. In: Hayes, D.E. (Ed.), The Tectonic and Geologic Evolution of Southeast Asian Seas and Islands (Part 2). In: Geophysical Monograph Series, vol. 27. American Geophysical Union, Washington, D. C, pp. 23–56.

Tibi, R., Wiens, D.A., Shiobara, H., Sugioka, H., Shore, P.J., 2006. Depth of the 660-km discontinuity near the Mariana slab from an array of ocean bottom seismographs. Geophys. Res. Lett. 33 (2), L02313. https://doi.org/10.1029/2005GL024523.

Van der Meijde, M., Marone, F., Giardini, D., Van der Lee, S., 2003. Seismic evidence for water deep in Earth's upper mantle. Science 300 (5625), 1556–1558. https://scite.ai/reports/10.1126/science.1083636.

Van der Voo, R., Spakman, W., Bijwaard, H., 1999. Tethyan subducted slabs under India. Earth Planet. Sci. Lett. 171 (1), 7–20. https://doi.org/10.1016/S0012-821X(99)00131-4.

van Keken, P.E., Hacker, B.R., Syracuse, E.M., Abers, G.A., 2011. Subduction factory: 4. Depth-dependent flux of H2O from subducting slabs worldwide. J. Geophys. Res., Solid Earth 116 (B1), B01401. https://doi.org/10.1029/2010JB007922.

Williams, Q., Revenaugh, J., 2005. Ancient subduction, mantle eclogite, and the 300 km seismic discontinuity. Geology 33 (1), 1–4. https://doi.org/10.1130/G20968.1.

Wu, J., Suppe, J., 2018. Proto-South China Sea plate tectonics using subducted slab constraints from tomography. J. Earth Sci. 29, 1304–1318.

Xu, Y., Wei, J., Qiu, H., Zhang, H., Huang, X., 2012. Opening and evolution of the South China Sea constrained by studies on volcanic rocks: preliminary results and a research design. Chin. Sci. Bull. 57 (24), 3150–3164. https://doi.org/10.1007/s11434-011-4921-1.

Yu, Y., Gao, S.S., Liu, K.H., Yang, T., Xue, M., Le, K.P., 2017. Mantle transition zone discontinuities beneath the Indochina Peninsula: implications for slab subduction and mantle upwelling. Geophys. Res. Lett. 44 (14), 7159–7167. https://doi.org/10.1002/2017GL073528.

Yu, Y., Gao, S.S., Liu, K.H., Zhao, D., 2020. Foundered lithospheric segments dropped into the mantle transition zone beneath southern California, USA. Geology 48 (2), 200–204. https://doi.org/10.1130/G46889.1.

Yu, Y., Song, J., Liu, K.H., Gao, S.S., 2015. Determining crustal structure beneath seismic stations overlying a low-velocity sedimentary layer using receiver functions. J. Geophys. Res., Solid Earth 120 (5), 3208–3218. https://doi.org/10.1002/2014JB011610.

Zahirovic, S., Müller, R.D., Seton, M., Flament, N., Gurnis, M., Whittaker, J., 2012. Insights on the kinematics of the India-Eurasia collision from global geodynamic models. Geochem. Geophys. Geosyst. 13 (4), Q04W11. https://doi.org/10.1029/2011GC003883.

Zenonos, A., De Siena, L., Widiyantoro, S., Rawlinson, N., 2019. P and S wave travel time tomography of the SE Asia-Australia collision zone. Phys. Earth Planet. Inter. 293, 106267. https://doi.org/10.1016/j.pepi.2019.05.010.

Zheng, Y., Lay, T., Flanagan, M.P., Williams, Q., 2007. Pervasive seismic wave reflectivity and metasomatism of the Tonga mantle wedge. Science 316 (5826), 855–859. https://www.jstor.org/stable/20036224.